High-power few-cycle THz generation at MHz repetition rates in an organic crystal

Tobias Olaf Buchmann, Edmund John Railton Kelleher, Mojca Jazbinsek, Binbin Zhou, Jin-Hong Seok, O-Pil Kwon, Fabian Rotermund, and Peter Uhd Jepsen

COLLECTIONS

F This paper was selected as Featured

View Online   Export Citation   CrossMark

ARTICLES YOU MAY BE INTERESTED IN

Terahertz transient stimulated emission from doped silicon
APL Photonics 5, 106102 (2020); https://doi.org/10.1063/5.0020654

A universal framework for microscope sensorless adaptive optics: Generalized aberration representations
APL Photonics 5, 100801 (2020); https://doi.org/10.1063/5.0022523

Tutorial: An introduction to terahertz time domain spectroscopy (THz-TDS)
Journal of Applied Physics 124, 231101 (2018); https://doi.org/10.1063/1.5047659

APL Photonics
SPECIAL TOPIC: Coronavirus and Photonics
Submit Today!

High-power few-cycle THz generation at MHz repetition rates in an organic crystal Ⓕ

View Online   Export Citation   CrossMark

Tobias Olaf Buchmann,[1,a] Ⓘⅅ Edmund John Railton Kelleher,[1,a] Ⓘⅅ Mojca Jazbinsek,[2] Ⓘⅅ Binbin Zhou,[1] Ⓘⅅ Jin-Hong Seok,[3] O-Pil Kwon,[3] Fabian Rotermund,[4] Ⓘⅅ and Peter Uhd Jepsen[1,a] Ⓘⅅ

AFFILIATIONS

[1] Department of Photonics Engineering, Technical University of Denmark, Ørsteds Plads 343, Kgs. Lyngby 2800, Denmark
[2] Institute of Computational Physics, Zurich University of Applied Sciences, Technikumstrasse 9, 8400 Winterthur, Switzerland
[3] Department of Molecular Science and Technology, Ajou University, 443-749 Suwon, South Korea
[4] Department of Physics, Korea Advanced Institute of Science and Technology (KAIST), 34141 Daejeon, South Korea

[a] Authors to whom correspondence should be addressed: toobu@fotonik.dtu.dk; edkel@fotonik.dtu.dk; and puje@fotonik.dtu.dk

ABSTRACT

Ultrafast terahertz (THz) spectroscopy is a potent tool for studying the fundamental properties of matter. Limitations of current THz sources, however, preclude the technique being applied in certain advanced configurations or in the measurement of, e.g., strongly absorbing samples. In response to this problem, here we demonstrate the generation of 1.38 mW broadband THz radiation at 10 MHz repetition rate by combining the highly efficient nonlinear organic crystal HMQ-TMS with ultrafast pump pulses generated using a simple and stable external pulse compression of a high power, near-infrared (NIR) femtosecond ytterbium-doped fiber (Yb:fiber) laser. Utilizing spectral broadening in a large core, polarization maintaining photonic crystal fiber and a pair of SF11 prisms, we achieve a tenfold pulse compression of the Yb:fiber laser, yielding compressed 0.35 μJ pulses with a full-width at half maximum pulse duration of 22 fs, exerting a peak power of 13.8 MW at a repetition rate of 10 MHz. THz generation through optical rectification of the NIR pulses is explored in two distinct thicknesses of the organic crystal, leading to a maximum conversion efficiency of ~$5.5 \cdot 10^{-4}$, an order of magnitude higher than that achieved with inorganic nonlinear crystals, e.g., gallium phosphide, for similar pump parameters. The focused THz beam has a peak on-axis field strength greater than 6.4 kV cm^{-1} in unpurged atmosphere. We believe that our moderately strong-field THz source is well suited to a variety of applications in ultrafast THz spectroscopy, in particular THz-enabled scattering-type near-field, and scanning tunneling spectroscopy, where multi-MHz repetition rate sources are required.

INTRODUCTION

Advances in the development of ultrafast laser-based generation of high intensity pulses in the terahertz (THz) range (0.2–30 THz) over the last two decades have enabled a wealth of new application areas in both fundamental and applied science.[1] In particular, time-domain and time-resolved time-domain spectroscopic techniques have proven a particularly powerful approach for the characterization of novel materials in physics, chemistry, and biology, as well as for uncovering the non-equilibrium dynamics in such material systems.[2] To this end, there has been a significant focus

placed on improving the operational bandwidth, source acquisition speed, peak field strength, and average power to extend the scope and improve the quality of possible studies. In addition, system complexity, cost, and overall footprint are important considerations for the translation of developments in THz sources into commercially viable technologies. Unfortunately, it is often the case that these attributes trade off against each other: for instance, enhancing the acquisition speed by increasing the source repetition rate reduces the per-pulse energy. This results in a consequent reduction in the peak field strength often preventing the use of the source in strong-field experiments that are an increasingly important research

pathway for understanding fundamental problems in the physics of condensed-matter systems.[3] Similarly, targeting a high peak field strength by adopting a high-energy (millijoule-class), femtosecond amplifier not only restricts the repetition frequency to the few-kilohertz range but also increases the overall system footprint, complexity, and cost. Consequently, the evolution of table-top, pulsed THz sources has been tightly coupled to advances in state-of-the-art ultrafast lasers offering high pulse energy at high repetition rates.

The generation of laser-driven pulsed THz radiation can be classified into two established schemes: generation by optically driven photoconductivity in a semiconductor target and generation through nonlinear optical processes. For the latter, optical rectification (OR)[4] and laser-driven gas-ionization[5] both depend on the manipulation of electron charge to generate a radiating transient charge current, while the so-called "spintronic"[6] emitters additionally exploit the spin properties of electrons through transient spin-to-charge transfer in magnetic multi-layer thin-films. Advanced photoconductive THz antennas, enhanced by plasmonic nanocavities, have offered impressive, high-power performance delivering up to 4 mW of average power at megahertz (MHz) repetition rates with just watt-level excitation,[7] but due to the necessary tight plasmonic confinement of the pump light, further power-scaling based on the fabrication of large-area devices could prove challenging. Nonlinear optical processes—both perturbative second-order effects in solid-state crystals and non-perturbative nonlinear interactions in gases leading to the generation of laser-driven plasmas—can routinely generate single-cycle THz transients with peak field strengths exceeding several MV cm^{-1}. Although plasma-based sources can cover an extremely broad bandwidth (up to and in excess of 40 THz) and even approach peak electric fields of 100 MV cm^{-1}, the driving laser requirements in the millijoule energy range currently prevent intense THz-plasma sources in the MHz regime.[8] Hence, the generation of intense THz radiation at MHz repetition rates is targeted through OR in solid-state crystals (a second-order, intra-pulse difference frequency mixing process). OR requires phase-matching between the near-infrared (NIR) driving pulse and the generated THz field to be efficient, and thus, the choice of the generation material must be carefully selected based on the availability of the pump system.

Currently, high average power, MHz repetition rate femtosecond lasers and amplifiers are dominated by ytterbium-doped (Yb-doped) technologies with emission around 1.03 μm. Due to intrinsic limitations of the gain medium, however, durations in the tens of femtosecond regime are not possible without external stages of post-compression. The application of ultrafast Yb-doped sources for power-scaling of THz radiation through OR has been pursued for more than a decade.[9,10] Although predicted as early as 2006,[9] milliwatt-level powers in single- or few-cycle THz transients at repetition rates in the multi-MHz regime utilizing high average power Yb-based pump sources have only very recently been demonstrated. For example, Meyer *et al.* have generated an average THz power of 1.35 mW at 13.4 MHz through OR in a 1 mm thick gallium phosphide (GaP) crystal, with a spectrum extending to 6 THz, when pumped by the compressed output of a Yb-doped thin-disk laser delivering an average power of 112 W (8.35 μJ) in a 88 fs pulse centered at 1.03 μm.[11] Furthermore, power-scaling to 66 mW of THz power using a very similar pump source (with a compressed

duration of 236 fs) has been achieved through OR in lithium niobate but with a bandwidth limited to ~2.5 THz.[12] Despite this record power at a high repetition rate, the narrow bandwidth of the generated THz pulses will limit applications of the source, particularly in experiments where the resonant excitation of specific low-energy modes of a material may require the source bandwidth to cover up to and beyond 10 THz. In addition, because of the high THz refractive index of lithium niobate, the added complexity of having to tilt the pulse intensity front of the driving laser to achieve efficient non-collinear velocity matching in the bulk crystal is undesirable and degrades the spatial circularity of the generated THz beam. The consideration of the modal properties of the generated THz radiation is particularly important for the application of the source in cutting-edge techniques such as THz-enabled scattering-type scanning near-field optical microscopy[13] and scanning tunneling microscopy (STM).[14] In both cases, a collinear generation scheme is a significant advantage, while a high repetition rate (>1 MHz) and a strong field are particularly important to ensure a sufficient signal-to-noise ratio in either application and to drive a measurable tunnel current in THz-STM. In our previous work,[15] we reported efficient, broadband, and intense THz generation at MHz repetition rates in the organic nonlinear optical crystal HMQ-TMS[20] [2-(4-hydroxy-3-methoxystyryl)-1-methylquinolinium 2,4,6-trimethylbenzenesulfonate] when pumped by the compressed output of a Yb:fiber laser, generating 0.38 mW of THz average power. The performance of the HMQ-TMS crystal as a THz emitter based on OR was compared against a GaP crystal and showed an order of magnitude enhancement for similar pump parameters due to the strong nonlinear index of the organic material. Due to the OR process being based on an intra-pulse difference frequency generation, both the generated THz bandwidth and NIR-THz conversion efficiency increase with decreasing NIR pulse duration; a shorter NIR pulse is thus beneficial. Here, we show that an optimization of the pulse compression together with an area scaling by loosening the pump focal spot size—while maintaining high fluence—allows the generation of milliwatt-level THz emission up to 6 THz bandwidth at 10 MHz repetition rate, with average pump powers in the few-watt range.

The dependence of THz generation on the input pump pulse duration is shown in Fig. 1(a), where we use an analytical approach based on Ref. 16 to evaluate the generated THz spectra from 0.25 mm thick HMQ-TMS as a function of the transform-limited (TL) pump pulse duration at an equal pump energy (and pump fluence) for every input. We adopt a non-depleted plane-wave pump approximation, account for the frequency dependent Fresnel transmission at each crystal–air interface, and use realistic material parameters, including the dispersion of the refractive index and absorption in the THz and optical range for HMQ-TMS.[17,18] We do not consider any spectral limitations due to THz wave propagation or detection. The model shows that the output spectral bandwidth scales favorably with a decreasing input pulse duration, showing higher frequency spectral components and an overall higher spectral amplitude compared to the output when pumped with longer pulses. For a clear comparison, all curves are normalized to the peak of the TL 20 fs trace. There is a remarkable enhancement to the generated spectra for pulse durations below 50 fs compared to 88 fs and 95 fs, the pulse durations used for optical rectification in GaP in Refs. 11 and 19. Furthermore, the reduced pulse duration allows for
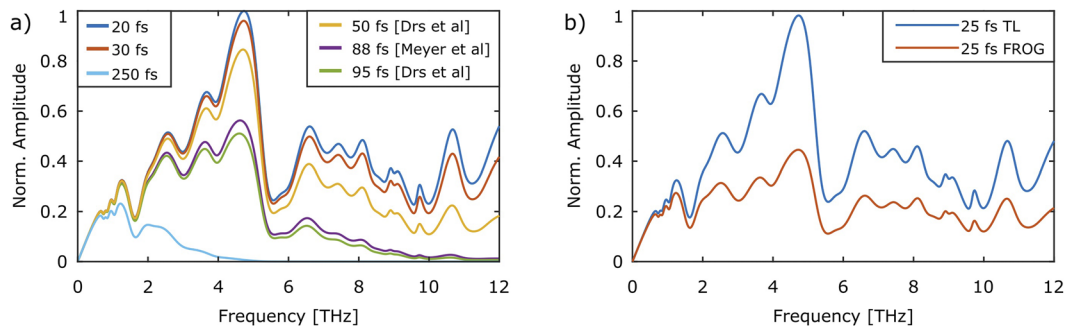
FIG. 1. (a) Modeled behavior of the generated THz spectra in 0.25 mm thick HMQ-TMS as a function of pump pulse duration considering TL optical pump pulses. All pump pulses are centered at 1.035 μm with equal pulse energy, normalized to the 20 fs spectrum. The modeling suggests an increased conversion efficiency for shorter pump pulses and an increased bandwidth. (b) The modeled spectral output for a TL 25 fs pulse (blue) compared to the experimentally measured 25 fs FROG trace (orange) as the input.

operation at a lower average thermal load while maintaining suitably high peak-powers, allowing for efficient operation in a non-critical thermal regime of the THz generation crystal. In Fig. 1(b), we compare the computed THz output when pumped with a TL 25 fs pulse to the expected output computed with our experimentally measured pump pulse, characterized using frequency-resolved optical gating (FROG). In this case, we also consider the same overall pulse energy of the TL 25 fs pulse and the experimentally measured pump pulse, assuming that the generated THz spectral amplitude is proportional to the Fourier transform of the pump intensity temporal profile.[16] The mentioned pulse and FROG results are discussed in detail in the sections titled Nonlinear pulse compression: scaling relations for solid-core fibers, Details of the experimental setup, and Results and discussion. The resulting difference in the generated spectra can be attributed to the fact that the experimental pulse contains ~60% of the total pulse energy in its main peak with a full-width at half maximum (FWHM) of 25 fs, with the remaining power lying in the low-intensity wings of the pulse, emphasizing the additional benefit that clean pulse compression offers. We restrict the computed spectral range to 12 THz based on the measured optical parameters of HMQ-TMS in this range.[17,18]

In the section titled Nonlinear pulse compression: scaling relations for solid-core fibers, we elaborate on the design considerations and optimization of the external nonlinear pulse compression (NPC), before discussing in detail the experimental system and outlining our results. We introduce a large mode area (LMA) polarization-maintaining (PM), solid-core photonic crystal fiber (PCF) with a 40 μm core diameter (LMA-40-PM-PCF) developed by NKT-Photonics. Spectral broadening in the PCF is followed by subsequent compression with a SF11 prism pair, yielding 22 fs pulses (a compression by approximately a factor of 10 compared to the output of the pump laser), resulting in a peak power of 13.8 MW. The compressed pulse is then optically rectified in the highly efficient nonlinear organic crystal HMQ-TMS to generate a multi-octave THz output, with 1.38 ± 0.06 mW of average power at 10 MHz repetition rate. We compare the impact of different HMQ-TMS crystal thicknesses subject to femtosecond pumping at 1.035 μm and a repetition rate of 10 MHz. Finally, we discuss a careful characterization of the calibrated peak on-axis field strength of the generated THz

emission. Our results suggest that the combination of Yb-doped femtosecond source technologies together with organic crystals could prove the most practical route for the generation and scaling of compact, broadband, high-power THz sources with high repetition rates suitable for targeting strong-field applications utilizing the latest THz-enabled spectroscopic techniques.

NONLINEAR PULSE COMPRESSION: SCALING RELATIONS FOR SOLID-CORE FIBERS

Nonlinear pulse compression (NPC) is a long-established technique for the generation of pulses with durations significantly shorter than can be directly generated from a mode-locked laser.[21,22] Briefly, self-phase modulation (SPM) can be exploited together with a dispersive delay element to obtain temporal compression of the original pulse envelope. Spectral broadening of NIR laser pulses through SPM in waveguides has the benefit over bulk media that it does not impose a spatial phase variation restricting the achievable compression factor.[23] In addition, optical fibers allow for maintaining high intensities over long propagation lengths, reducing the pump laser requirements for efficient nonlinear broadening of the input spectrum. Standard optical fibers such as small-core single-mode fibers, however, impose a strict limit on the power and energy scalability of the architecture due to their low optical damage threshold. The advent of the photonic crystal fiber[24,25] laid the foundations for LMA optical fibers that can maintain robust single-mode operation and tolerate peak powers above 2 MW,[26] approaching the self-focusing power for fused silica glass.[27] Single-mode LMA PCFs thus represent a convenient platform for use in a high-power NPC scheme.[26,28]

For NPC with optical fibers, group velocity dispersion (GVD) has a defining role on the evolution of the pulse-shape throughout the spectral broadening process. The influence of GVD is particularly pronounced for NPC of femtosecond pulses because of the broader initial input bandwidth.[22] When the GVD is positive (i.e., normally dispersive), the effect temporally broadens the pulse envelope, adding to the accumulation of positive chirp. Positive GVD is typical for LMA PCFs in the wavelength region around the gain bandwidth of Yb-doped laser amplifiers centered at 1.03 μm as the

waveguide dispersion approaches that of the bulk glass for increasing core-size. Importantly, this dispersive broadening acts to linearize the SPM-induced chirp profile that is otherwise only linear over the central portion of the pulse with maximum intensity, effectively re-shaping the pulse in time such that the envelope is close to rectangular.[28–30] This leads to a superior quality of the compressed output pulse when it is de-chirped by an anomalously dispersive delay element, minimizing the presence of sidelobes in the temporal domain, but also sets the fiber length as a critical parameter. An expression for the optimum fiber length was introduced in Ref. 29 based on extensive numerical analysis,

$$L_{\mathrm{opt}} \approx \sqrt{6 L_{\mathrm{D}} L_{\mathrm{NL}}}, \tag{1}$$

where $L_{\mathrm{D}} = \frac{T_0^2}{|\beta_2|}$ is the dispersion length and $L_{\mathrm{NL}} = (\gamma P_{\mathrm{peak}})^{-1}$ is the nonlinear length. To convert the pulse width T_0 defined as the half-width at $1/e$ intensity to intensity at FWHM, we use the relation $T_{\mathrm{FWHM}} = T_0 \cdot 2 \ln(1 + \sqrt{2})$ for temporally sech^2-shape pulses.[31] The GVD is β_2, the peak power is P_{peak}, and $\gamma = 2\pi n_2/(\lambda A_{\mathrm{eff}})$ is the nonlinear parameter assuming a material nonlinear refractive index n_2 and a modal effective area A_{eff}. Intuitively, one might choose the input peak power just below the fiber-specific damage threshold. The approximate relationship for the optimal fiber length given by Eq. (1), however, is based on a nonlinear Schrödinger model that neglects nonlinear effects that become relevant for pulses significantly shorter than 1 ps while also considering the influence only of second-order rather than higher-orders of the dispersion. For our experimental conditions, the most dominant additional nonlinearities observed in solid-core silica fibers are optical wave-breaking (OWB) and stimulated inelastic Raman scattering (SRS), which are both known to have a negative impact on quadratic pulse compression.[32,33] In Fig. 2(a), we plot the optimal fiber length given by Eq. (1) (orange-shaded band) and the characteristic length where SRS becomes significant (blue-shaded band). For the estimation of the optimal length given by Eq. (1), the bounds correspond to the dispersion parameters for bulk fused silica (lower limit) and that of LMA-25 (upper limit)—a PCF similar to the LMA-40-PM-PCF, but with a smaller core diameter of 25 μm. This band therefore provides

a good estimate of the performance expected for LMA-40-PM-PCF. For calculation of the characteristic Raman length, we use a scaling model[34,35] allowing for a reliable estimate of the Raman gain coefficient at the center wavelength of the pump laser and an expression relevant for passive LMA fibers introduced in Ref. 36. We set the Raman threshold at 1% of the input pump power, as proposed for the operation of fiber amplifiers.[37] The range of literature values for the Raman gain coefficient of fused silica, e.g., $0.80 \cdot 10^{-13}$ m W^{-1} in Ref. 38 and $0.99 \cdot 10^{-13}$ m W^{-1} in Ref. 39, lead to the upper and lower boundaries of the band shown in Fig. 2(a), respectively. When considering the influence of SRS on short pulses, the effective nonlinear interaction length should be taken into account depending on the walk-off length governed by the pulse duration and the dispersive properties of the fiber. Shorter pulses and more dispersive media will yield a shorter walk-off length. For a 250 fs input pulse centered at a wavelength of 1.035 μm, the peak of the Raman Stokes wave is red-shifted by ~50 nm (a frequency shift of 13.2 THz resulting from the peak Raman gain in fused silica), the corresponding walk-off length estimated for LMA-40-PM-PCF (assuming bulk silica values of the dispersion) is thus on the order of 8.5 cm. Comparing the three length-scales, the optimum fiber length given by Eq. (1), the characteristic Raman length, and the walk-off length, it is clear that the input peak-power yielding optimal broadening for pulse compression lies below the damage threshold of the fiber [vertical line at 2.1 MW in Fig. 2(a)] in the range around a peak power of 1.5 MW, corresponding to a fiber length of ~14 cm. In fact, we confirm empirically that the best compression is achieved at an operating peak power of 1.41 MW and a fiber length of 13.5 cm, closely matching the intersection region of the curves in Fig. 2(a). To confirm the role of the Raman contribution on the evolution of the input pulse in the chosen optimal fiber length, we perform a numerical simulation for our experimental parameters. We assume a TL input pulse with a FWHM duration of 250 fs and a corresponding peak power matching our operating condition. The numerical simulation is based on a generalized nonlinear Schrödinger model of the pulse propagation.[40] With a fractional Raman contribution of 18% (typical for silica fibers), small modulations to the temporal intensity appear on the leading edge of the pulse after 13.5 cm propagation
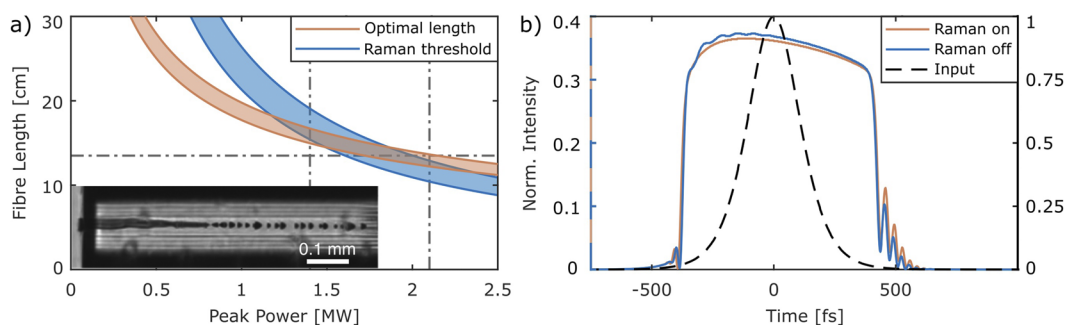
FIG. 2. (a) Optimal fiber length (shaded orange) and characteristic Raman length (shaded blue) as a function of the input peak power, each framed by its uncertainty range. Vertical dashed lines show the empirically confirmed optimal operating peak power (1.41 MW) and the fiber damage threshold (2.1 MW), respectively. The horizontal line lies at the fiber length of 13.5 cm. The inset shows an optical microscope image of the PCF after irreversible damage due to a fiber-fuse. (b) Temporal profiles of the numerically simulated input pulse (dashed black) after propagating through 13.5 cm of fiber, corresponding to the optimal experimental operating conditions, with (blue curve) and without (orange curve) the influence of Raman nonlinearity.

[see Fig. 2(b)]. The effect, however, is weak in comparison to the stronger modulations particularly prominent on the trailing edge of the pulse that we attribute to OWB.

DETAILS OF THE EXPERIMENTAL SETUP

Figure 3 shows a sketch of the experimental setup divided into the external pulse compression and the THz-generation with electro-optical sampling (EOS) detection. For the compression stage, the p-polarized output of the Yb:fiber laser (250 fs, 10 MHz) is sent through a fivefold beam expander followed by a variable attenuator consisting of a half-wave plate and a polarizing beam splitter set to transmit 8.63 W. The enlarged beam with a $1/e^2$ diameter of ~7 mm is re-focused with a 200 mm air-spaced doublet to a spot size closely matching the 32 μm mode field diameter of the LMA-40-PM-PCF. The fiber is installed on a three-axis translation stage and rotationally oriented such that the polarization of the pump light is either perpendicular or parallel to the stress rods in order to preserve the p-polarization at the output (see inset I in Fig. 3 for an optical image of the fiber end-face). The spectrally broadened output from the fiber is collimated with a 50 mm achromatic lens and sent through a double-pass SF11 equiangular prism-pair compressor, with the back-propagating beam at a slight vertical displacement in order to direct the compressed beam out of its original beam path with a pickoff mirror. The majority of the compressed output is used to pump the THz emitter, while a small portion is picked off for analysis and monitoring of the pulse properties including the pulse length, spectrum, and power, using the following instruments: an interferometric autocorrelator (IAC), FROG, a spectrum analyzer, and a power meter.

External pulse compression

Yb-doped pump laser

We use an early prototype version of the upgraded and commercially available Aeropulse-FS series from NKT Photonics. The laser emits a linearly polarized beam with >23 dB extinction ratio at a center wavelength of 1.035 μm and a spectral bandwidth of 8 nm. Internal dispersion control allows the sech²-shaped output

pulses to be adjusted from 250 fs to 1 ps duration (FWHM). The output repetition rate can be set at distinct intervals over the range 2 MHz–20 MHz, corresponding to integer divisions of the internal oscillator fundamental frequency, allowing for pulse energies up to 22 μJ at a maximum output power of 44 W. The spatial properties of the output beam are characterized by an M^2 value of <1.2, a beam divergence of 1.8 mrad, and an output diameter at $1/e^2$ of 0.8 mm. The above parameters are given by the initial test report conducted by NKT after installation of the laser. From our own measurements, we verify the long-term stability of these parameters.

LMA-40-PM-PCF

The LMA-40-PM-PCF has three key features: single-mode guidance in the NIR, polarization preservation, and a large core allowing for high average power handling. These properties negate the effects of inter-modal and polarization mode dispersion. Thus, pulse propagation is approximated as scalar with the coupled power lying in the fundamental mode. Due to its large core size and consequently diminishing contribution to the total dispersion from the waveguide, the dispersive properties of the fiber can be approximated by the material dispersion of bulk fused silica with the GVD = 18.6 fs² mm⁻¹ at the wavelength of 1.035 μm. We achieve a coupling efficiency into the core mode of ~50%, which we determine by separating unwanted cladding-guided light with the use of a Wollaston prism before measuring the power of the purely p-polarized output in the far field without a collimating lens. We assume a negligible contribution to the total transmission from attenuation, in line with reported losses for other LMA PCFs of less than 5 dB/km in the NIR range. The power-handling capacity was evaluated over a range of repetition rates in the MHz regime, proving to be constant for a given peak-power. We conclude a damage threshold of 2.1–2.2 MW, at which point the core of the fiber is irreversibly damaged due to the fiber-fuse effect repeatedly initiating at the point of the first fiber-clamp (for a deeper analysis of the fiber fuse damage process and external effects on the point of initiation, we refer the reader to Ref. 41). The resulting damage shows a regular "bullet-shaped" destruction pattern characteristic of femtosecond pulsed fiber fuses [see the inset of Fig. 2(a)]. This value is con-
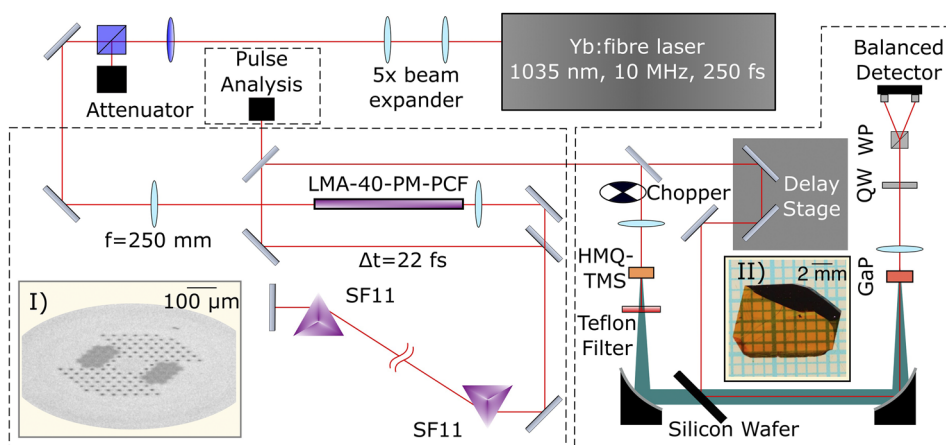
FIG. 3. Overview of the experimental setup that can be separated into the compression stage and the THz generation stage with subsequent detection through EOS. We compress 250 fs pulses to 22 fs. Insets I and II show the front-facet of the PCF (microscope image) and the crystal HMQ-TMS for illustrative purpose, respectively.

sistent with the core-size dependent damage thresholds reported in Ref. 26 and lies at roughly 50% of the self-focusing threshold of fused silica, as predicted in Ref. 27. An important treatment of the fiber is the prior removal of the polymer-coating at the input end, otherwise the coating has a tendency to burn due to absorbed cladding light, again resulting in permanent damage of the fiber. Similarly, the fiber-clamp acts as a "hotspot" for inducing damage, so the removed polymer section should extend beyond the fiber clamp. We find that the core coupling efficiency and the fiber damage threshold are both reduced with increased clamping pressure, which necessitates an "as soft as possible" approach to fix the fiber in position.

Dispersion compensating prism-pair

We use equiangular prisms of SF11 glass due to its high dispersion and the possibility to fine-tune the dispersion compensation. The larger third-order dispersion (TOD) compared to SF10 glass also improves the quality of the compressed pulse (i.e., reduced temporal wings), owing to greater compensation of residual positive TOD accumulated in the laser oscillator, amplifier, and broadening fiber. Furthermore, large aperture SF11 prisms accommodating the full spatially dispersed beam without clipping are affordable and readily available. We empirically find the optimum prism separation that supports the minimum pulse duration, yielding a group delay dispersion compensation of ~6200 fs^2 (assuming a 5 mm beam insertion in the second prism). This is achieved first with a coarse sweep of the prism separation to find the region of minimum duration (resulting in ~45 cm), followed by varying the insertion of the second prism for fine-tuning (while monitoring the FROG trace). Overall loss for the double-pass compressor configuration is ~8%, which we mainly attribute to the beams not being exactly at Brewster's angle over the entire bandwidth (in particular the back-propagating light due to the 60° apex of the prisms preventing Brewster's angle on both prism interfaces). Since only p-polarized light is maximally transmitted, the polarization purity is also further enhanced after the prism compressor.

NIR pulse analysis

The pulse duration is measured with a home-built IAC. Silver steering mirrors and ultra-thin beam splitters are used to minimize dispersion in the beam path between the compressor output and the point of measurement. The two collinear beams are then focused with an off-axis paraboloidal silver mirror onto a GaAsP photodiode, where a time-dependent two-photon induced photo-current is recorded[42] by an oscilloscope (Tektronix MDO3104), mapping out the characteristic IAC trace [see the inset of Fig. 4(a)]. The phase information of the compressed pulse is retrieved through the measurement of the second-harmonic FROG trace using a commercial device (Mesa Photonics) with a 100 μm thick barium borate crystal. The optical spectrum is recorded by an integrating sphere fiber coupled to an optical spectrum analyzer (ANDO:AQ6317B), while the NIR power is measured with a thermal power meter (Thorlabs S350C), and the polarization is verified with a Wollaston prism. To determine the pulse-to-pulse stability of the pump laser and the possible introduction of intensity noise after the NPC stage, we conducted spectrally resolved relative intensity noise (RIN) measurements using a large bandwidth (5 GHz) photodiode (Thorlabs:DET08CFC) and a fast (4 GHz) real-time oscilloscope (Teledyne:LeCroy-HD09404).[43,44]

THz generation and detection

HMQ-TMS crystal

THz generation through OR is achieved by optically pumping the nonlinear organic crystal HMQ-TMS[20] with the compressed NIR pulses. HMQ-TMS is a promising alternative to GaP in the wavelength region around 1.03 μm, compatible with Yb-doped laser technology. The electro-optic coefficient of HMQ-TMS[45] is ~50 pm V^{-1} (measured at 633 nm), 50 times larger than that of GaP,[46] although the refractive index mismatch between the NIR and THz range necessitates the use of comparatively thinner crystals.[15] We analyze two samples of different thickness: ~0.25 mm and 0.45 mm. As observed with all organic crystals, HMQ-TMS
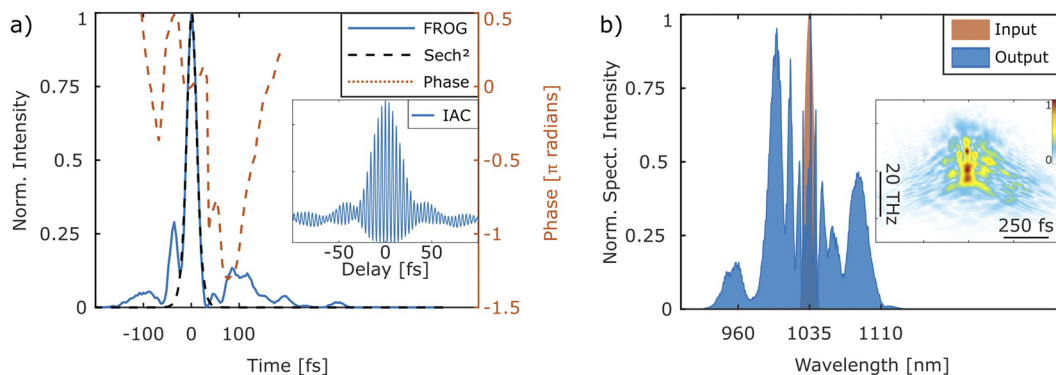
FIG. 4. (a) Retrieved FROG trace (blue) with sech^2-fit to the main peak (black, FWHM 25 fs) containing ~60% of the pulse energy. The remaining energy is contained in pre- and post-pulses, resulting from residual higher-order phase components. The near-flat phase across the main pulse demonstrates close to optimal compression. The inset shows the recorded IAC trace, showing the optical cycles of the pulse (FWHM 22 fs). (b) NIR input spectrum (orange) and broadened spectrum (blue), both normalized to their respective peak. The peak Raman-gain is expected at 1084 nm. We attribute the spectral feature below 960 nm to OWB. The inset shows the retrieved FROG trace.

possesses a low optical damage threshold (1.8–3.6 mJ cm^{-2} for MHz operation[15]) compared to inorganic THz crystals but can be prepared as large-area crystals by a simple cleaving method,[20] allowing for an increased pump beam area at high average power, while remaining below the required fluence threshold.

THz waveform: sampling and characterization

The main beam output from the compressor is split into a low-power (mW-level) "probe" and a high-power "pump" beam. The 3 W pump beam is sent through a variable reflective attenuator and then focused into the HMQ-TMS crystal with a 250 mm focal length lens to a spot size at $1/e^2$ of ~0.17 mm in diameter. Based on the estimation of the dispersion introduced by additional optical elements in the beam path after the compressor, the pulse duration at the HMQ-TMS crystal is expected to be ~25 fs. The peak fluence illuminating the generation crystal is controlled by moving the crystal around the focal point using a 25 mm range linear translation stage. After the THz emitter, the THz beam is collimated with a 2 in. focal length paraboloidal mirror and the majority of the residual NIR power is removed using strongly scattering strips of 75 μm thin PTFE (Teflon), each transmitting ~89% of the THz radiation. Following this, the THz beam and the delayed probe beam are then overlapped via a high-resistivity silicon wafer mounted at 45°, transmitting the THz and reflecting the probe beam. The collinearly propagating beams are subsequently focused with a 3 in. focal length paraboloidal mirror into a 0.3 mm thick GaP detection crystal, where the time-varying electric field of the THz pulse induces a birefringence, which in turn changes the polarization of the probe beam. Hence, the THz field is written into the polarization of the probe beam, which is detected as an imbalance on a balanced photodetector (Newport 2107-FS) after passing a quarter-wave plate and a Wollaston prism, while lock-in detection is used to minimize the background. Due to constraints of the specific beam path, the setup is not purged with nitrogen.

For measurements of the generated THz average power, we use a calibrated pyro-electric detector (Gentec-EO) positioned in place of the detection crystal, while the probe beam is blocked. We pay particular attention to minimize the residual NIR contribution by applying a set of filters after the generation crystal. These consist of two 75 μm thin PTFE strips (THz transmission of 89% each, strongly scattered IR transmission of 5% measured directly behind the filter), a normal incidence high-resistivity silicon wafer with 0.525 mm thickness (THz transmission of 47%, IR transmission of 11%), and a 45° angled silicon wafer (34% THz transmission, 15% IR transmission). The relative humidity (RH) in the laboratory has a seasonal variation between 20% and 30%, which corresponds to an absorption coefficient for our relevant THz spectral range of 0.74 m^{-1} (lower bound) and 0.92 m^{-1} (upper bound), respectively. With a THz beam path (from generation to detection crystal) of ~45 cm, the total RH (30%–20%) related THz transmission lies between 63% and 69%, which we correct for when calculating the total generated power and conversion efficiency, leading to an average value within a given uncertainty range.

The THz transmission values for the individual filters are measured with an in-house broadband THz system (extending to 30 THz[47]) and extracted for the relevant spectral range of 0.25 THz–5.5 THz, while the NIR attenuation (at 1.035 μm) was measured using an optical power meter. Furthermore, the use of stacked silicon wafers was avoided since the transmission function is sensitive to the angular alignment of consecutive wafers and is not given by the simple 0.5^n approximation.[48] To eliminate any remaining non-THz contributions to the THz power measurement, we move the HMQ-TMS crystal far out of focus (i.e., significantly decreasing the pump intensity and thus the generated THz signal) and record the power reading. This value is then deducted from the THz power measurements. The focused THz spot size is recorded with an uncooled micro-bolometer (NEC THz Imager IR/V-T0831) with a pixel size of 25.5 μm. The peak power of the NIR pump pulse is calculated using a pre-factor of 0.88 to compensate for the sech^2 temporal shape of the pulse, while peak intensities based on a Gaussian spatial profile are calculated using $I_{peak} = 2 \cdot P_{peak}/(\pi w^2)$, with the spot diameter $2w$ defined at $1/e^2$ intensity.

RESULTS AND DISCUSSION

Pulse compression

The IAC (inset) and FROG trace are shown in Fig. 4(a) with the shortest IAC measured FWHM pulse duration being 22 fs. The reconstructed temporal pulse from the FROG measurement shows a small residual linear chirp across the main pulse, which contains ~60% of the pulse energy. The FROG measurement yields a slightly longer pulse-duration than the IAC trace (~25 fs) due to its non-collinear scheme, limited phase-matching bandwidth, and the additional need to use a half-wave plate, which cannot offer equal retardance over the entire bandwidth of the NIR pulse. The residual FROG error is 0.0177, where the FROG error is the root mean square difference between the measured and retrieved traces divided by the number of points in the trace. The presence of sidelobes in the FROG trace are attributed to uncompensated TOD accumulated in the pump laser and not fully compensated by the quadratic compressor, as well as higher-order phase contributions from OWB and SRS. Figure 4(b) shows the measured output bandwidth in comparison to the input bandwidth, which is approximately tenfold broader at ~90 nm FWHM and shows the characteristic SPM modulations, as well as a prominent feature near 960 nm, which we attribute to OWB. In terms of compression ratio and pulse duration, our system compares to similar approaches using LMA-PCFs in combination with Yb-doped laser sources operating at multi-watt power levels and MHz repetition rates that report pulse durations between 19 fs and 33 fs.[49–51] With 3.45 W of power output from the compressor, we have a total NPC power-loss of ~60%, the majority of which (86%) is due to fiber-coupling loss alone. This results in a peak-power of 13.8 MW—nearly a tenfold enhancement over 1.4 MW coupled into the fiber, with a key advantage of this particular PCF being that the pulse maintains its input polarization. Collapsing the fiber-ends of the PCF with a splicing filament in order to improve the coupling due to the reduced numerical aperture mismatch did not yield an improvement in the coupling efficiency. By varying the fiber input power and repetition rate, we find that the optimized fiber length for the compression remains the same when maintaining the same pulse energy and subsequently the same peak power. Once aligned, the setup runs stably and can be considered "turn-key" with no adjustments required for daily operation. Over longer periods of

time, slight optimization to the fiber coupling is necessary to mitigate slow drifts in the alignment. Since this approach is peak-power limited, scaling of the average power with repetition rates can be readily achieved. The source laser RIN was measured to be 1.07%, whereas the compressed output has an average RIN across its full bandwidth of 1.71%, suggesting only a relatively small noise contribution from the nonlinear spectral broadening process. Spectrally resolving the RIN by filtering the peripheral red- and blue-shifted frequency components (i.e., bandwidth outside the range 1.0 μm–1.08 μm) results in a reduced RIN value ~1.5%, indicating greater noise contributions at the spectral edges.

THz-wave generation

Figures 5(a) and 5(b) show the calibrated time-dependent THz electric-field recorded using EOS and the corresponding spectral power density, respectively, when pumping 0.25 mm (blue) and 0.45 mm (orange) thick HMQ-TMS crystals with 22 fs, 0.25 μJ pulses (1.25 W of average power) and a pump focal spot size of 0.17 mm (1/e^2 diameter). The single pulse energy is calculated based on the full (un-chopped) average NIR pump power. Throughout the operation of the system and measurement of the generated THz radiation, the pump beam is optically chopped at 673 Hz (for lock-in detection), reducing the overall thermal load by a factor of two and preventing irreversible damage to the crystal. It can be seen that the stronger peak field is achieved with the 0.25 mm thick crystal. For the thicker 0.45 mm crystal, the spectrum shows increased power at a low frequency and reduced power at a higher frequency, while the overall spectral power is ~80% of the spectral power generated with the 0.25 mm crystal. We also observe an overall lower damage threshold for the thicker crystal, which we attribute to higher absorption due to the extended interaction length. The efficiency difference is also noted in the time-domain as a lower recorded peak field strength of ~5.3–5.4 kV cm^{-1} compared to ~6.3–6.4 kV cm^{-1} for the 0.25 mm crystal. In both cases, the

generated spectra spans almost 6 THz at −20 dBm THz^{-1}. The atmospheric absorption lines due to water-vapor at a RH of 25% (based on spectroscopic data from the HITRAN database) are plotted in Fig. 5(b) to show the strong correlation with features present in the THz spectra. The on-axis field strength is calibrated using E_{cal} = $\Gamma \cdot E_{raw}$ with the scaling factor Γ. To determine the scaling factor, we use the relation for the pulse energy U given by the integral of the intensity, $U = \int_{-\infty}^{\infty} dx \int_{-\infty}^{\infty} dy \int_0^T I(x,y,t)dt$. The spatial dimensions x and y are defined as the radius at 1/e^2 intensity of a Gaussian beam, and thus, the spatial expression becomes $I(x,y) = \exp\left(-\frac{2x^2}{w_x^2} - \frac{2y^2}{w_y^2}\right)$, where w_x and w_y are the Gaussian beam widths. Applying the spatial Gaussian integral $\int_{-\infty}^{\infty} \int_{-\infty}^{\infty} \exp(-ax^2 - by^2)dxdy = \frac{\pi}{\sqrt{a}\sqrt{b}}$ and the relation between the intensity and the field $I(t) = c\varepsilon_0 n \int_0^T E(t)^2 dt$, one can simplify to $U = \frac{\pi w_x w_y c\varepsilon_0 n}{2} \int_0^T E(t)^2 dt$. It is important to note that the often used relation $I = \frac{c\varepsilon_0 n}{2}|E_0|^2$ only holds for a time-averaged sinusoidal electric field. Together with the relation of power, repetition rate, and energy $U = \frac{P}{f_{\text{rep}}}$, the scaling factor Γ is given by

$$\Gamma = \sqrt{\frac{2P}{f_{\text{rep}} c\varepsilon_0 n\pi w_x w_y \int_0^T E_{raw}(t)^2 dt}}, \qquad (2)$$

where $c = 2.998 \cdot 10^8$ m s^{-1} is the speed of light in vacuum, $\varepsilon_0 = 8.85$ pF m^{-1} is the vacuum permittivity, and $n \sim 1$ is the refractive index of air. To calculate the field strength with this method, one requires the corresponding THz pulse energy (calculated from the recorded THz average power P and repetition rate f_{rep}), the measured THz focal spot size (with assumed Gaussian intensity distribution), and the integral of the measured EOS-trace, which can be computed through $\sum |E_{raw}|^2 \Delta t$ with the EOS time step Δt.

Through analyzing Eq. (2), it becomes clear that the calibration factor is sensitive only to the shape of the EOS trace, not its amplitude, while the measured beam spot and the filter-adjusted average THz power are the other value sensitive input parameters.
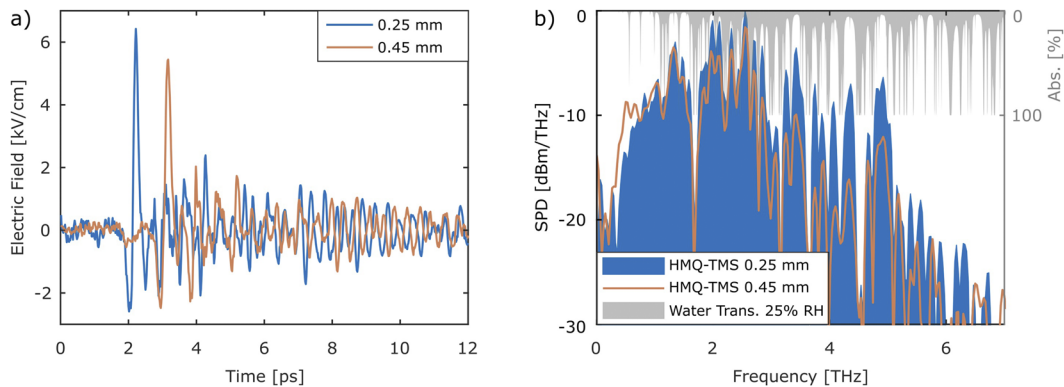
FIG. 5. (a) Calibrated time traces of the generated THz electric field emitted from HMQ-TMS of different thicknesses, spanning 10 ps (0.25 mm crystal, blue) and 9 ps (0.45 mm crystal, orange), reaching more than 6 kV cm^{-1} peak on-axis field strengths. The oscillations result from the interaction with water-vapor in the atmosphere. (b) Output spectral power density (SPD) after propagation through ~45 cm of air at ~25% RH. The thin crystal of 0.25 mm (shaded blue) shows stronger high-frequency components, while the 0.45 mm crystal (orange) offers a low-frequency increase below 1 THz, but with the overall spectral power lying at ~80% of the thin crystal. The humidity dependent absorption at 25% RH (gray) matches the corresponding dips in the spectrum.

Distinct from other schemes, this makes the calibration of the THz field strength using this approach less sensitive to the alignment of the probe and THz beams in the EOS detection. One must, however, pay careful attention to filter corrections, i.e., the input THz power P should not be compensated for any loss effects that affect the shape of the EOS trace, such as humidity related losses. A drawback of this method is the assumption of the measured average THz power being proportional to the recorded EOS trace, which overestimates the field-strength when taking time-limited EOS traces (up to several tens of picoseconds), while the power reading records an average including the contributions of all echoes and water ringing. In theory, for accurate calculation of the field strength, one would therefore require very long EOS-traces spanning the duration between two pulses, which in practice is often impractical. The generation crystal echoes are expected after 3.3–3.8 ps for the thin crystal and 6.0–6.9 ps for the thick crystal (the range arising from the uncertainty thickness of the HMQ-TMS crystals). Both of these echo contributions are therefore included within the experimentally measured EOS trace spanning ~10 ps and ~9 ps for the thin and thick crystal traces, respectively (although not prominent in our recorded data due to the more dominant water ringing). On the other hand, echoes lying outside of this time window, such as those resulting from the Si-wafer, are not included in the EOS trace (occurring after 16–17 ps for 0.525 mm thick wafers mounted at 45°) but contribute to the average power recorded by the power meter. Through the analysis of EOS traces in a separate purged setup, we conclude that the power contribution of the Si-wafer echoes lies at ~7.5%. Similarly, contributions from the water-ringing fall below 1% only after ~60 ps at 20% RH. The EOS trace of the thin crystal is missing 13.5% (19.0%) of the total power at 20% (30%) RH, while the thick crystal due to the shorter duration of 9 ps is missing 14.7% (21.0%). Hence, the integral of the EOS trace in Eq. (2) needs to be corrected to adjust for this, reducing the correction factor Γ by the square root of that respective value. Finally, the noise in the EOS trace recorded before the onset of the THz pulse should be excluded from the calibration.

The input values resulting in the ~6.4 kV cm^{-1} peak on-axis peak field strength for the thin crystal at 20% RH are the filter and echo-corrected average THz power $P = 0.904$ mW at 2.50 W input pump power and a repetition rate of $f_{\text{rep}} = 10$ MHz (where the power value is not compensated for humidity loss since our recorded trace is taken at ambient conditions). The focused Gaussian waist radii at $1/e^2$ for the thin crystal at 20% RH are $w_x = 0.25$ mm and $w_y = 0.77$ mm, with the strong ellipsoid here resulting from the off-axis paraboloidal mirror focusing characteristics and non-optimal alignment. Our thin crystal conversion efficiency is $5.5 \pm 0.2 \cdot 10^{-4}$, which is significantly larger than has been reported for GaP with similar pump parameters (at ~$0.15 \cdot 10^{-4}$ in Refs. 11 and 19). For the efficiency calculation, we use the total generated THz power $P = 1.38 \pm 0.06$ mW, which is corrected for humidity losses, the uncertainty arising from the RH spread of 20%–30%. The thick crystal efficiency is slightly lower at $3.3 \pm 0.1 \cdot 10^{-4}$. By placing the experimental setup in a dry atmosphere, and by reducing the THz spot size with tighter focusing, peak on-axis field strengths beyond 20 kV cm^{-1} in a few-cycle THz pulse at MHz repetition rates are well within reach. Such a high repetition rate source capable of delivering these field strengths would greatly benefit, for example, broadband THz-STM measurements, where

tip-induced low-pass filtering inhibits the instrument's high frequency response.[52]

CONCLUSION

We have demonstrated milliwatt-level, few-cycle THz pulse generation at 10 MHz repetition rate by combining Yb-doped fiber laser technology, an external pulse compression based on a polarization maintaining LMA solid-core PCF, and the organic nonlinear optical crystal HMQ-TMS. We achieve efficient, broadband emission extending up to 6 THz with a peak on-axis field strength of 6.4 kV cm^{-1} and a transient duration of 200 fs (defined as the time between the leading maximum and minimum of the THz waveform). The nonlinear pulse compression scheme comprises spectral broadening in LMA-40-PM-PCF and subsequent compression with an SF11 prism pair for a FWHM duration of 22 fs. The scalability of this approach is limited by the damage threshold of the solid-core fiber, which could be circumvented by moving to a hollow-core fiber platform.[53] With a pump peak power of ~9 MW on the THz generation crystal, we achieve a NIR-to-THz conversion efficiency of ~$5.5 \cdot 10^{-4}$, significantly higher than has been reported for other THz sources based on OR of Yb-doped systems in inorganic crystals, e.g., GaP. The unique properties of our THz source make it well suited to a number of time-resolved spectroscopic applications, in particular scattering-type, scanning near-field, and scanning-tunneling techniques, where high repetition rates and field strengths are required.

DATA AVAILABILITY

The data that support the findings of this study are available from the corresponding author upon reasonable request.

REFERENCES

[1]S. S. Dhillon, M. S. Vitiello, E. H. Linfield, A. G. Davies, M. C. Hoffmann, J. Booske, C. Paoloni, M. Gensch, P. Weightman, G. P. Williams, E. Castro-Camus, D. R. S. Cumming, F. Simoens, I. Escorcia-Carranza, J. Grant, S. Lucyszyn, M. Kuwata-Gonokami, K. Konishi, M. Koch, C. A. Schmuttenmaer, T. L. Cocker, R. Huber, A. G. Markelz, Z. D. Taylor, V. P. Wallace, J. Axel Zeitler, J. Sibik, T. M. Korter, B. Ellison, S. Rea, P. Goldsmith, K. B. Cooper, R. Appleby, D. Pardo, P. G. Huggard, V. Krozer, H. Shams, M. Fice, C. Renaud, A. Seeds, A. Stöhr, M. Naftaly, N. Ridler, R. Clarke, J. E. Cunningham, and M. B. Johnston, "The 2017 terahertz science and technology roadmap," J. Phys. D: Appl. Phys. **50**, 043001 (2017).

[2]P. U. Jepsen, D. G. Cooke, and M. Koch, "Terahertz spectroscopy and imaging—Modern techniques and applications," Laser Photonics Rev. **5**, 124–166 (2011).

[3] T. Kampfrath, K. Tanaka, and K. A. Nelson, "Resonant and nonresonant control over matter and light by intense terahertz transients," Nat. Photonics **7**, 680–690 (2013).

[4] S. L. Dexheimer, *Terahertz Spectroscopy: Principles and Applications* (CRC Press, 2017).

[5] J. A. Fueloep, S. Tzortzakis, and T. Kampfrath, "Laser-driven strong-field terahertz sources," Adv. Opt. Mater. **8**, 1900681 (2019).

[6] T. Seifert, S. Jaiswal, U. Martens, J. Hannegan, L. Braun, P. Maldonado, F. Freimuth, A. Kronenberg, J. Henrizi, I. Radu, E. Beaurepaire, Y. Mokrousov, P. M. Oppeneer, M. Jourdan, G. Jakob, D. Turchinovich, L. M. Hayden, M. Wolf, M. Münzenberg, M. Kläui, and T. Kampfrath, "Efficient metallic spintronic emitters of ultrabroadband terahertz radiation," Nat. Photonics **10**, 483–488 (2016).

[7] N. T. Yardimci, S. Cakmakyapan, S. Hemmati, and M. Jarrahi, "A high-power broadband terahertz source enabled by three-dimensional light confinement in a plasmonic nanocavity," Sci. Rep. **7**, 4166 (2017).

[8] J. Buldt, M. Mueller, H. Stark, C. Jauregui, and J. Limpert, "Fiber laser-driven gas plasma-based generation of THz radiation with 50-mW average power," Appl. Phys. B **126**, 2 (2020).

[9] G. Chang, C. J. Divin, C.-H. Liu, S. L. Williamson, A. Galvanauskas, and T. B. Norris, "Power scalable compact THz system based on an ultrafast Yb-doped fiber amplifier," Opt. Express **14**, 7909–7913 (2006).

[10] M. C. Hoffmann, K.-L. Yeh, H. Y. Hwang, T. S. Sosnowski, B. S. Prall, J. Hebling, and K. A. Nelson, "Fiber laser pumped high average power single-cycle terahertz pulse source," Appl. Phys. Lett. **93**, 141107 (2008).

[11] F. Meyer, N. Hekmat, T. Vogel, A. Omar, S. Mansourzadeh, F. Fobbe, M. Hoffmann, Y. Wang, and C. J. Saraceno, "Milliwatt-class broadband THz source driven by a 112 W, sub-100 fs thin-disk laser," Opt. Express **27**, 30340 (2019).

[12] F. Meyer, T. Vogel, S. Ahmed, and C. J. Saraceno, "Single-cycle, MHz repetition rate THz source with 66 mW of average power," Opt. Lett. **45**, 2494–2497 (2020).

[13] X. Chen, D. Hu, R. Mescall, G. You, D. N. Basov, Q. Dai, and M. Liu, "Modern scattering-type scanning near-field optical microscopy for advanced material research," Adv. Mater. **31**, 1804774 (2019).

[14] T. L. Cocker, V. Jelic, M. Gupta, S. J. Molesky, J. A. J. Burgess, G. D. L. Reyes, L. V. Titova, Y. Y. Tsui, M. R. Freeman, and F. A. Hegmann, "An ultrafast terahertz scanning tunnelling microscope," Nat. Photonics **7**, 620–625 (2013).

[15] T. O. Buchmann, E. J. R. Kelleher, K. J. Kaltenecker, B. Zhou, S.-H. Lee, O.-p. Kwon, M. Jazbinsek, F. Rotermund, and P. U. Jepsen, "MHz-repetition-rate, sub-mW, multi-octave THz wave generation in HMQ-TMS," Opt. Express **28**, 9631–9641 (2020).

[16] A. Schneider, M. Neis, M. Stillhart, B. Ruiz, R. U. A. Khan, and P. Günter, "Generation of terahertz pulses through optical rectification in organic DAST crystals: Theory and experiment," J. Opt. Soc. Am. B **23**, 1822–1835 (2006).

[17] C. Vicario, B. Monoszlai, M. Jazbinsek, S. H. Lee, O. P. Kwon, and C. P. Hauri, "Intense, carrier frequency and bandwidth tunable quasi single-cycle pulses from an organic emitter covering the terahertz frequency gap," Sci. Rep. **5**, 14394 (2015).

[18] F. D. J. Brunner, S.-H. Lee, O.-P. Kwon, and T. Feurer, "THz generation by optical rectification of near-infrared laser pulses in the organic nonlinear optical crystal HMQ-TMS," Opt. Mater. Express **4**, 1586 (2014).

[19] J. Drs, N. Modsching, C. Paradis, C. Kränkel, V. J. Wittwer, O. Razskazovskaya, and T. Südmeyer, "Optical rectification of ultrafast Yb lasers: Pushing power and bandwidth of terahertz generation in GaP," J. Opt. Soc. Am. B **36**, 3039 (2019).

[20] J. H. Jeong, B. J. Kang, J. S. Kim, M. Jazbinsek, S. H. Lee, S. C. Lee, I. H. Baek, H. Yun, J. Kim, Y. S. Lee, J. H. Lee, J. H. Kim, F. Rotermund, and O. P. Kwon, "High-power broadband organic THz generator," Sci. Rep. **3**, 3200 (2013).

[21] A. Laubereau, "External frequency modulation and compression of picosecond pulses," Phys. Lett. A **29**, 539–540 (1969).

[22] A. S. L. Gomes, A. S. Gouveia-Neto, and J. R. Taylor, "Optical fibre-grating pulse compressors," Opt. Quantum Electron. **20**, 95–112 (1988).

[23] N. Milosevic, G. Tempea, and T. Brabec, "Optical pulse compression: Bulk media versus hollow waveguides," Opt. Lett. **25**, 672–674 (2000).

[24] T. A. Birks, J. C. Knight, and P. S. J. Russell, "Endlessly single-mode photonic crystal fiber," Opt. Lett. **22**, 961–963 (1997).

[25] J. Broeng, D. Mogilevstev, S. E. Barkou, and A. Bjarklev, "Photonic crystal fibers: A new class of optical waveguides," Opt. Fiber Technol. **5**, 305–330 (1999).

[26] M. Seidel, X. Xiao, and A. Hartung, "Solid-core fiber spectral broadening at its limits," IEEE J. Sel. Top. Quantum Electron. **24**, 1 (2018).

[27] A. V. Smith, B. T. Do, G. R. Hadley, and R. L. Farrow, "Optical damage limits to pulse energy from fibers," IEEE J. Sel. Top. Quantum Electron. **15**, 153–158 (2009).

[28] T. Eidam, F. Röser, O. Schmidt, J. Limpert, and A. Tünnermann, "57 W, 27 fs pulses from a fiber laser system using nonlinear compression," Appl. Phys. B **92**, 9–12 (2008).

[29] W. J. Tomlinson, R. H. Stolen, and C. V. Shank, "Compression of optical pulses chirped by self-phase modulation in fibers," J. Opt. Soc. Am. B **1**, 139–149 (1984).

[30] G. P. Agrawal, *Applications of Nonlinear Fiber Optics*, 2nd ed. (Academic Press, 2008).

[31] G. P. Agrawal, *Nonlinear Fiber Optics*, 5th ed. (Academic Press, 2007).

[32] T. Nakashima, M. Nakazawa, K. Nishi, and H. Kubota, "Effect of stimulated Raman scattering on pulse-compression characteristics," Opt. Lett. **12**, 404–406 (1987).

[33] E. A. Golovchenko, E. M. Dianov, P. V. Mamyshev, and A. M. Prokhorov, "Optical fibre-grating pulse compression," Opt. Quantum Electron. **20**, 343–355 (1988).

[34] F. A. Oguama, H. Garcia, and A. M. Johnson, "Simultaneous measurement of the Raman gain coefficient and the nonlinear refractive index of optical fibers: Theory and experiment," J. Opt. Soc. Am. B **22**, 426 (2005).

[35] L. Gruner-Nielsen, Y. Qian, and P. B. Gaarde, "Fiber Bragg gratings for dispersion compensation in optical communication systems," J. Opt. Fiber Commun. Rep. **3**, 61–89 (2006).

[36] C. Jauregui, J. Limpert, and A. Tünnermann, "On the Raman threshold of passive large mode area fibers," Proc. SPIE **7914**, 791408 (2011).

[37] C. Jauregui, J. Limpert, and A. Tünnermann, "Derivation of Raman threshold for CW double-clad fiber amplifiers," Opt. Express **17**, 8476–8490 (2009).

[38] T. Nakashima, S. Seikai, and M. Nakazawa, "Dependence of Raman gain on relative index difference for GeO$_2$-doped single-mode fibers," Opt. Lett. **10**, 420–422 (1985).

[39] C. Lin, L. G. Cohen, R. H. Stolen, G. W. Tasker, and W. G. French, "Near-infrared sources in the 1–1.3 μm region by efficient stimulated Raman emission in glass fibers," Opt. Commun. **20**, 426–428 (1977).

[40] E. J. R. Kelleher, J. C. Travers, S. V. Popov, and J. R. Taylor, "Role of pump coherence in the evolution of continuous-wave supercontinuum generation initiated by modulation instability," J. Opt. Soc. Am. B **29**, 502–512 (2012).

[41] R. Kashyap, "The fiber fuse—From a curious effect to a critical issue: A 25th year retrospective," Opt. Express **21**, 6422 (2013).

[42] J. K. Ranka, A. L. Gaeta, A. Baltuska, M. S. Pshenichnikov, and D. A. Wiersma, "Autocorrelation measurement of 6-fs pulses based on the two-photon-induced photocurrent in a GaAsP photodiode," Opt. Lett. **22**, 1344–1346 (1997).

[43] C. Lafargue, J. Bolger, G. Genty, F. Dias, J. M. Dudley, and B. J. Eggleton, "Direct detection of optical rogue wave energy statistics in supercontinuum generation," Electron. Lett. **45**, 217 (2009).

[44] R. D. S. Shreesha, R. D. Engelsholm, I. B. Gonzalo, B. Zhou, P. Bowen, P. M. Moselund, O. Bang, and M. Bache, "Ultra-low-noise supercontinuum generation with a flat near-zero normal dispersion fiber," Opt. Lett. **44**, 2216–2219 (2019).

[45] M. Jazbinsek, U. Puc, A. Abina, and A. Zidansek, "Organic crystals for THz photonics," Appl. Sci. **9**, 882 (2019).

[46] J. Lu, S.-H. Lee, X. Li, S.-C. Lee, J.-H. Han, O.-P. Kown, and K. A. Nelson, "Efficient terahertz generation in highly nonlinear organic crystal HMB-TMS," Opt. Express **26**, 30786 (2018).

[47] A. T. Tarekegne, B. Zhou, K. Kaltenecker, K. Iwaszczuk, S. Clark, and P. U. Jepsen, "Terahertz time-domain spectroscopy of zone-folded acoustic phonons in 4H and 6H silicon carbide," Opt. Express **27**, 3618 (2019).

[48] K. J. Kaltenecker, E. J. R. Kelleher, B. Zhou, and P. U. Jepsen, "Attenuation of THz beams: A "how to" tutorial," J. Infrared, Millimeter, Terahertz Waves **40**, 878–904 (2019).

[49] I. Pupeza, D. Sánchez, J. Zhang, N. Lilienfein, M. Seidel, N. Karpowicz, T. Paasch-Colberg, I. Znakovskaya, M. Pescher, W. Schweinberger, V. Pervak,

E. Fill, O. Pronin, Z. Wei, F. Krausz, A. Apolonski, and J. Biegert, "High-power sub-two-cycle mid-infrared pulses at 100 MHz repetition rate," Nat. Photonics **9**, 721–724 (2015).

[50] C. Jocher, T. Eidam, S. Hädrich, J. Limpert, and A. Tünnermann, "Sub 25 fs pulses from solid-core nonlinear compression stage at 250 W of average power," Opt. Lett. **37**, 4407–4409 (2012).

[51] T. Südmeyer, F. Brunner, E. Innerhofer, R. Paschotta, K. Furusawa, J. C. Baggett, T. M. Monro, D. J. Richardson, and U. Keller, "Nonlinear femtosecond pulse compression at high average power levels by use of a large-mode-area holey fiber," Opt. Lett. **28**, 1951–1953 (2003).

[52] M. Müller, N. Martín Sabanés, T. Kampfrath, and M. Wolf, "Phase-resolved detection of ultrabroadband THz pulses inside a scanning tunneling microscope junction," ACS Photonics **7**, 2046–2055 (2020).

[53] F. Köttig, D. Schade, J. R. Koehler, P. S. J. Russell, and F. Tani, "Efficient single-cycle pulse compression of an ytterbium fiber laser at 10 MHz repetition rate," Opt. Express **28**, 9099 (2020).